



HAL
open science

Crystallization behavior of N -doped Ge-rich GST thin films and nanostructures: An in-situ synchrotron X-ray diffraction study

O. Thomas, C. Mocuta, M. Putero, M.-I. Richard, P. Boivin, F. Arnaud

► **To cite this version:**

O. Thomas, C. Mocuta, M. Putero, M.-I. Richard, P. Boivin, et al.. Crystallization behavior of N -doped Ge-rich GST thin films and nanostructures: An in-situ synchrotron X-ray diffraction study. *Microelectronic Engineering*, 2021, 244-246, pp.111573. 10.1016/j.mee.2021.111573 . hal-03609171

HAL Id: hal-03609171

<https://hal.science/hal-03609171>

Submitted on 15 Mar 2022

HAL is a multi-disciplinary open access archive for the deposit and dissemination of scientific research documents, whether they are published or not. The documents may come from teaching and research institutions in France or abroad, or from public or private research centers.

L'archive ouverte pluridisciplinaire **HAL**, est destinée au dépôt et à la diffusion de documents scientifiques de niveau recherche, publiés ou non, émanant des établissements d'enseignement et de recherche français ou étrangers, des laboratoires publics ou privés.

Crystallization behavior of N -doped Ge-rich GST thin films and nanostructures: an *in-situ* synchrotron x-ray diffraction study

O. Thomas^{a*}, C. Mocuta^b, M. Putero^a, M.-I. Richard^{a,c}, P. Boivin^d, F. Arnaud^e

^a Aix-Marseille Université, CNRS, IM2NP UMR 7334, Campus de St-Jérôme, 13397 Marseille Cedex 20, France

^b Synchrotron SOLEIL, l'Orme des Merisiers, Saint-Aubin–BP 48, 91192 Gif-sur-Yvette, France

^c ID01/ESRF, The European Synchrotron, 71 rue des Martyrs, 38043 Grenoble, France

^dSTMicroelectronics, 190 Ave Coq, 13106 Rousset, France

^e STMicroelectronics, 850 rue Jean Monnet, 38920 Crolles, France

Abstract

Ge-rich and N-doped Ge-Sb-Te thin films and patterned structures for memory applications are investigated *in situ* during annealing up to 500°C with a heating rate of 2°C/min using synchrotron x-ray diffraction. The initial material is amorphous. Under these annealing conditions, Ge crystallization occurs at 340°C and precedes the one of cubic Ge₂Sb₂Te₅ by about 15°C. *In situ* monitoring of diffraction allows for a quantification of crystallized quantity, grain size and elastic strain during the material transformation. Increasing N doping reduces the amount of crystallized Ge and Ge grain size. These results bring important insights into the multiphase crystallization of Ge-rich GST phase change materials for memory applications.

Introduction

Phase Change Materials (PCM) are very promising for non-volatile memory applications [1-4]. Indeed, they can be switched reversibly very quickly between an amorphous and a crystal phase. In addition, the very high resistivity contrast between the two phases allows easy reading. One of the most studied PCM is $\text{Ge}_2\text{Sb}_2\text{Te}_5$ (commonly named GST in the literature), which has a crystallization temperature close to 150-170°C. This temperature is too low for long-enough data retention in many applications (*e.g.* automotive). Compositionally optimized Ge-rich GST (named θ -phase in the following) on the other hand has a crystallization temperature of about 350°C [5]. N-doping is commonly used in PCMs as a tool to reduce mechanical stresses related to crystallization, increase crystallization temperature or change the electrical resistance [6-9]. In this work, we investigate the crystallization behavior of confined θ -phase structures with *in-situ* synchrotron x-ray diffraction performed at the DiffAbs beamline of SOLEIL synchrotron. In addition the influence of N-doping on the crystallization process is evaluated.

Experimental conditions

Samples were *in situ* annealed under nitrogen atmosphere thanks to an Anton Paar® heating stage. The maximum annealing temperature was 500°C and the heating and cooling rate were respectively set to 2°C/min and 20°C/min. The furnace was mounted on the six-circle diffractometer (Kappa geometry) of the DiffAbs beamline at SOLEIL synchrotron. The beam size was $205 \times 255 \mu\text{m}^2$ (FWHM, $V \times H$). The XRD patterns were recorded in vertical geometry at a fixed incident angle $\omega = 8^\circ$ (yielding a beam footprint on the sample surface: $1473 \times 255 \mu\text{m}^2$) using a two-dimensional x-ray hybrid pixel array detector, XPAD [10]. An incident photon energy $E = 18 \text{ keV}$ was chosen in order to measure a large reciprocal space range. The diffracted intensities as a function of the diffracted angles 2θ were obtained after 1D azimuthal integration and by applying geometrical and flatfield corrections [11]. In this work, we have investigated four different samples. The first two ones (W9 and W11) are encapsulated (with silicon nitride) samples with POR (Process of Reference) N doping. W11 is a blanket film (50 nm) and W9 is an array of parallel lines with 50 nm width and 120 nm pitch prepared in the same conditions. The two others are encapsulated patterned samples with different N doping levels: W1 is POR-2%N and W12 is POR+2%N. They are summarized in Table 1. Line arrays are arranged in two parallel rectangles ($7 \times 4 \text{ mm}^2$ separated by 1 mm).

Sample	Morphology	N-doping
W11	blanket	POR
W1	patterned	POR-2%
W9	patterned	POR
W12	patterned	POR+2%

Table 1: List of investigated samples.

Experimental results

1°) W11 thin film (POR)

The complete room-temperature diffraction patterns (obtained by patching three detector positions) before annealing and after complete thermal cycling are shown in figure 1.

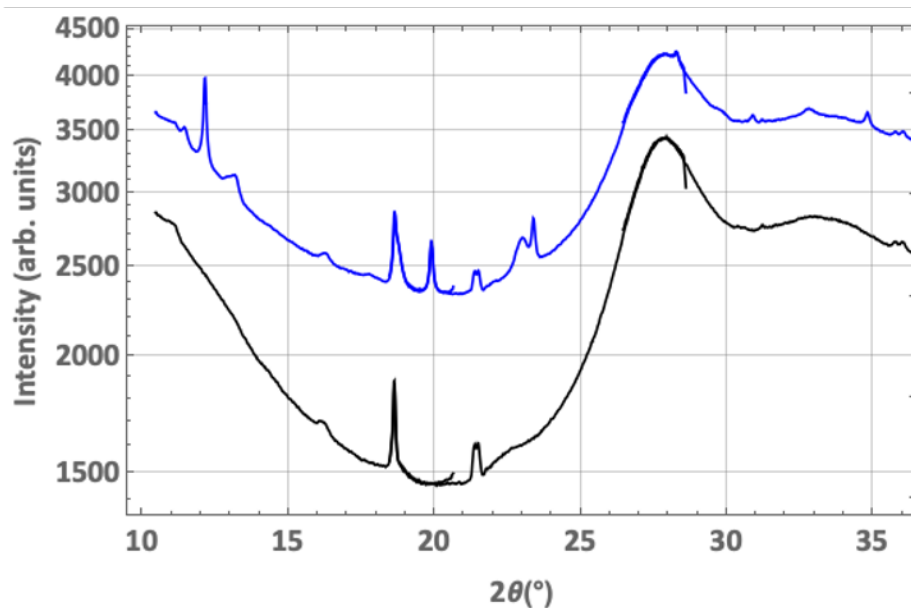


Figure 1: Room temperature diffraction patterns from sample W11 (POR thin film): before annealing (black); after annealing (blue). This latter one has been shifted for clarity.

In the pattern recorded prior to any heat treatment some peaks may arise from the sample holder / heating plate (at 18 keV the x-ray photons are only weakly absorbed by the silicon substrate). In addition, the broad bump centered around 28° is most probably diffuse scattering arising from the single crystal (001) Si substrate. After annealing the diffraction pattern exhibit distinct diffraction peaks, which witness crystallization of several phases. Figure 2 (a) shows the superimposition of the experimental diffraction pattern with powder diffraction data from $\text{Ge}_2\text{Sb}_2\text{Te}_5$ metastable cubic phase [12] and pure Ge. This comparison allows one to conclude that most of the diffraction peaks can be associated with these two phases. It is worth noting, however, a weak shoulder on the low-angle side of cubic GST 200 that may be attributed to the 013 (hexagonal indexation) peak of trigonal $\text{Ge}_2\text{Sb}_2\text{Te}_5$ stable phase [12]. Figure 2 (b) shows the indexation of the low angle peaks. In the same way the whole diffraction pattern may be indexed (not shown). From this indexation one may conclude that the annealed sample is a mixture of cubic Ge and cubic GST.

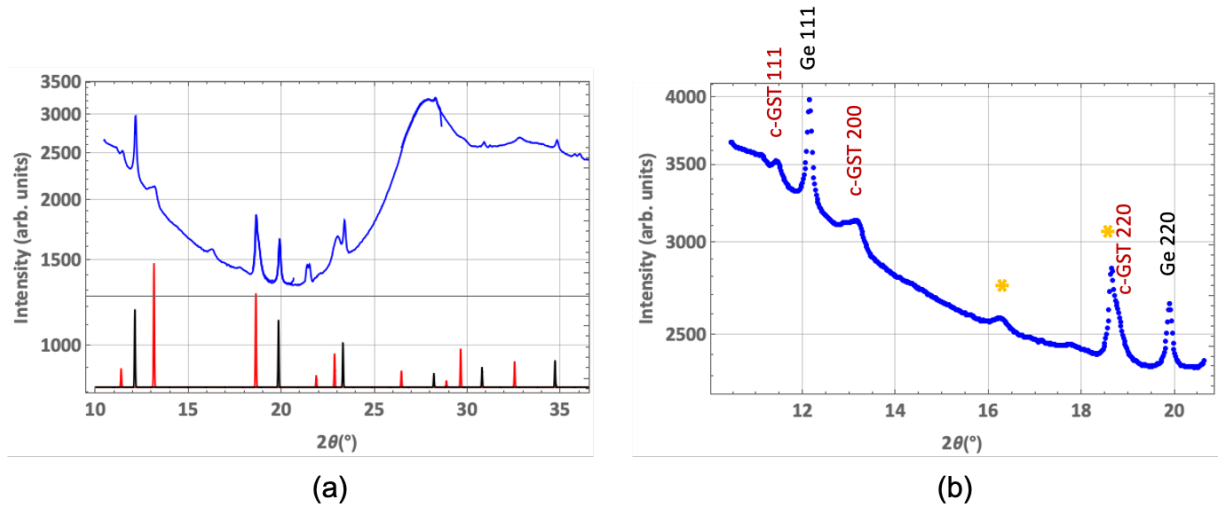


Figure 2: Room temperature diffraction pattern from sample W11 (POR thin film) after thermal cycling: (a) comparison with powder diffraction patterns from Ge (black) and cubic GST 225 (red); (b) indexation of the low angle part of the diffractogram. Stars indicate peaks which are already present in the unannealed sample (see figure 1).

These different diffraction peaks have been monitored as a function of temperature during the *in-situ* heating and cooling stages. Each peak has been fitted with a Pseudo-Voigt function and a linear background, which allows one to extract the following parameters: maximum intensity, peak position, full-width at half maximum (FWHM), peak area (integrated intensity).

The evolution of the integrated intensity of Ge 111 and GST 200 peaks as a function of temperature is shown in figure 3.

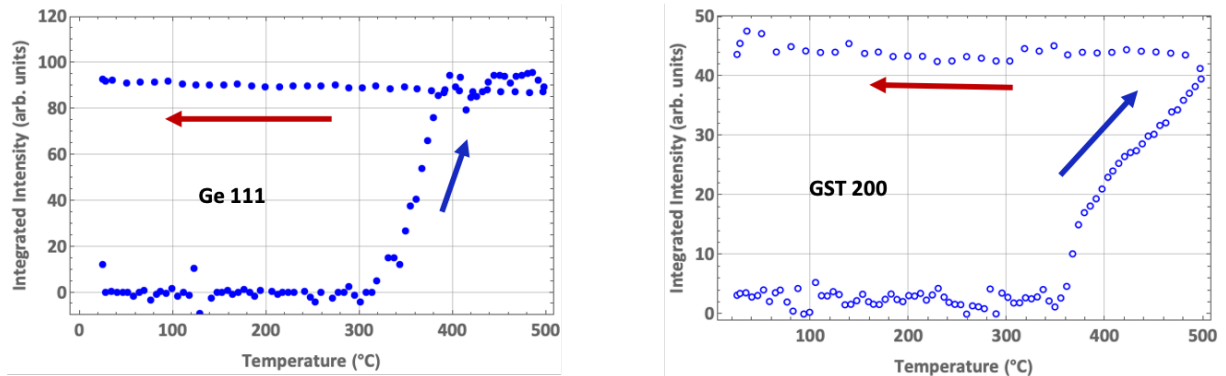


Figure 3: Integrated intensity of Ge 111 and GST 200 as a function of temperature for sample W11 (POR thin film). Blue arrows are for heating and red arrows for cooling.

Crystallization of Ge occurs at 340°C whereas crystallization of GST appears at a slightly higher temperature (355°C). In addition the two crystallization processes look very different: (i) abrupt in Ge; (ii) abrupt and then more progressive (two stages) in GST. Whereas the integrated intensity is related to the amount of diffracting material, the FWHM is inversely related (neglecting microstrain contributions) to the crystal size (along the direction of the scattering vector, which in the present case is roughly the normal to the film). The evolution of domain size as a function of temperature is shown in figure 4 both for Ge 111 and GST 200. The comparison of figure 3 and figure 4 for Ge 111 shows that Ge crystallization is

followed by grain growth, most probably via Ostwald ripening. In the case of GST 200, the apparent decrease in domain size is probably an artefact caused by the neglecting of microstrains. At around 480°C a weak shoulder on the low-angle side of cubic GST 200 appears. This additional signal may be attributed to the 013 (hexagonal indexation) peak of trigonal $\text{Ge}_2\text{Sb}_2\text{Te}_5$ stable phase.

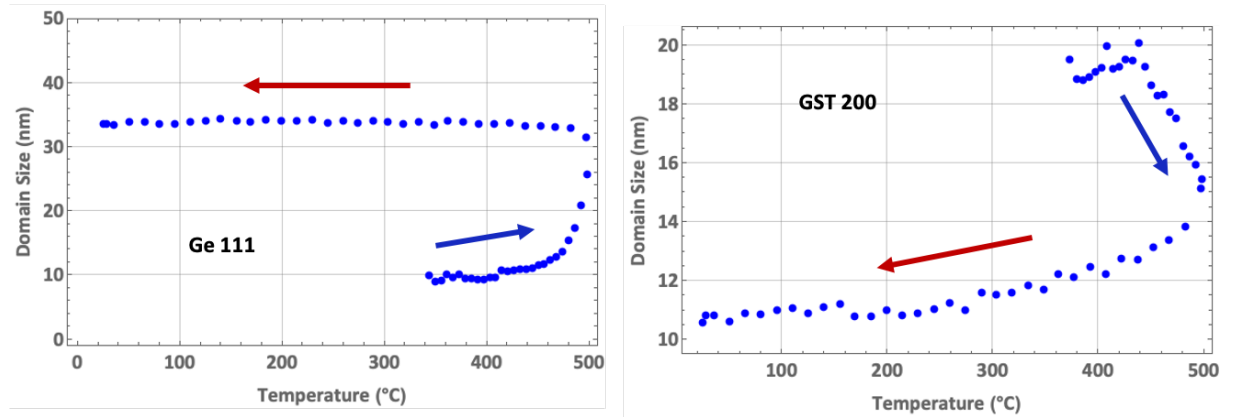


Figure 4: Domain size for Ge 111 and GST 200 (extracted from the FWHM of diffraction peaks) as a function of temperature for sample W11 (POR thin film). Blue arrows are for heating and red arrows for cooling.

The evolution of interplanar distances $d^{\text{Ge}_{111}}$ and $d^{\text{GST}_{200}}$ as a function of temperature is shown in figure 5. Upon cooling the linear behavior is characteristic of a thermoelastic loading and one may extract an effective perpendicular thermal expansion coefficient: $\alpha^{\text{Ge}_{\text{eff}}} = 9.9 \times 10^{-6} \text{ K}^{-1}$ and $\alpha^{\text{GST}_{\text{eff}}} = 19.6 \times 10^{-6} \text{ K}^{-1}$. Comparison of these values with known thermal expansion coefficients for Ge ($5.7 \times 10^{-6} \text{ K}^{-1}$) [13] and for GST ($17.4 \times 10^{-6} \text{ K}^{-1}$) [14] points to the existence of elastic strains (especially in Ge) resulting from thermal expansion mismatch with the Si substrate and/or between the two phases.

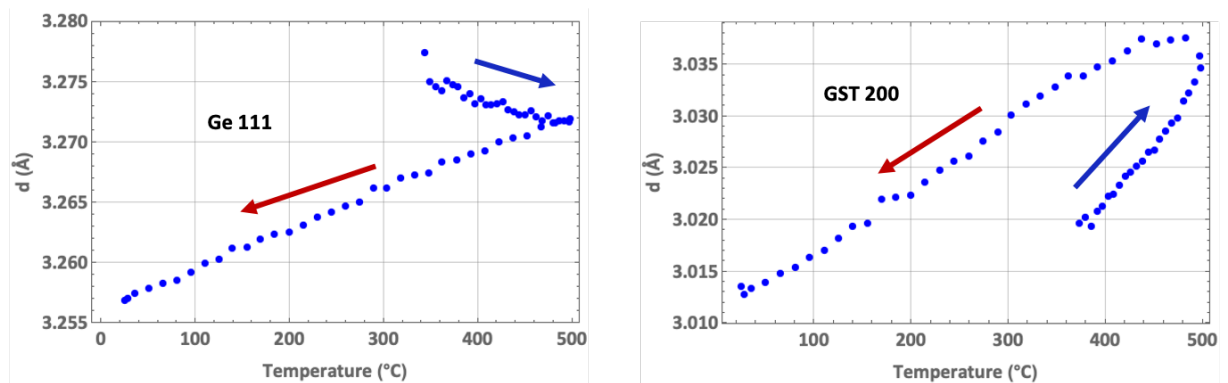


Figure 5: Evolution of interplanar distances $d^{\text{Ge}_{111}}$ and $d^{\text{GST}_{200}}$ as a function of temperature for sample W11 (POR thin film). Blue arrows are for heating and red arrows for cooling.

A summary of the results is given in tables 2 and 3. In the case of Ge a Williamson-Hall plot [15] yields a domain size of 49 nm and a microstrain of 0.26%. The room-temperature Ge lattice parameter refined from the values in table 2 is 0.56431 nm, i.e. -0.31 % smaller than the one from bulk unstrained Ge (0.56578 nm). Neglecting elastic anisotropy in Ge (which is mild with a Zener ratio of 1.6) and considering a Poisson ratio (ν) of 0.33 the perpendicular

effective thermal expansion coefficient of a Ge film (thermal expansion coefficient α_f) supported on a rigid substrate (thermal expansion coefficient α_s) is given by the following expression [16]:

$$\alpha_{eff}^{\perp} = \frac{1+\nu}{1-\nu} \alpha_f - \frac{2\nu}{1-\nu} \alpha_s \quad (1)$$

With $\alpha_f = 5.7 \times 10^{-6} \text{ K}^{-1}$ (Ge) [13] and $\alpha_s = 2.6 \times 10^{-6} \text{ K}^{-1}$ (Si) one gets $\alpha_{eff}^{\perp} = 9. \times 10^{-6} \text{ K}^{-1}$, close to the measured value of the order of $10. \times 10^{-6} \text{ K}^{-1}$.

hkl	d (nm)	q (nm ⁻¹)	Δq (nm ⁻¹)	Size RT (nm)	α_{eff} (10 ⁻⁶ K ⁻¹)
111	0.3256	19.30	0.187	34	9.93
220	0.1995	31.49	0.195	32	10.25
311	0.17	36.96	0.225	28	10.7
224	0.1152	54.54	0.274	23	9.77

Table 2: Summary of crystallographic parameters obtained in Ge at room temperature after thermal cycling in sample W11 (thin film POR). q is the modulus of the scattering vector. α_{eff} is the effective thermal expansion coefficient calculated from a linear fitting of d-spacing vs T upon cooling. The thermal expansion coefficient of Ge is $5.7 \times 10^{-6} \text{ K}^{-1}$.

The situation for GST is more complex. A Williamson-Hall plot is not realistic (negative domain size) and the effective thermal expansion coefficient varies a lot. It is hypothesized that the elastic anisotropy of GST (Zener ratio of 0.5 [17]) may play an important role in these results. The measured values may be compared with the effective thermal expansion coefficients for:

(i) a GST precipitate in a Ge matrix: $25. \times 10^{-6} \text{ K}^{-1}$, where a spherical precipitate (thermal expansion coefficient α_p) in an infinite matrix (thermal expansion coefficient α_m) is assumed, both media sharing the same isotropic elastic properties [18]:

$$\alpha_{eff} = \frac{2}{3} \frac{2-\nu}{1-\nu} \alpha_p - \frac{1}{3} \frac{1+\nu}{1-\nu} \alpha_m \quad (2)$$

(ii) a GST film on a Si substrate (calculated from eq. (1)): $32. \times 10^{-6} \text{ K}^{-1}$.

hkl	d (nm)	q (nm ⁻¹)	Δq (nm ⁻¹)	Size RT (nm)	α_{eff} (10 ⁻⁶ K ⁻¹)
111	0.34498	18.21	0.2699	23	27.34
200	0.3013	20.85	0.5924	11	19.6
200	0.2998	20.96	0.3837	16	30.09
222	0.17289	36.34	0.7456	8	26.87

Table 3: Summary of crystallographic parameters obtained in GST at room temperature after thermal cycling in sample W11 (thin film POR). q is the modulus of the scattering vector. α_{eff} is the effective thermal expansion coefficient calculated from a linear fitting of d-spacing vs T upon cooling. The thermal expansion coefficient of GST is $17.4 \times 10^{-6} \text{ K}^{-1}$.

2°) W9 patterned sample (POR)

Sample W9 has the same composition as sample W11 but is patterned. This results in a very significant drop in diffracted intensity as is shown in figure 6, which displays the intensity of the Ge 111 peaks in W11 and W9 after complete thermal cycling. This highly reduced intensity even for the strongest peak makes the *in-situ* analysis much more challenging.

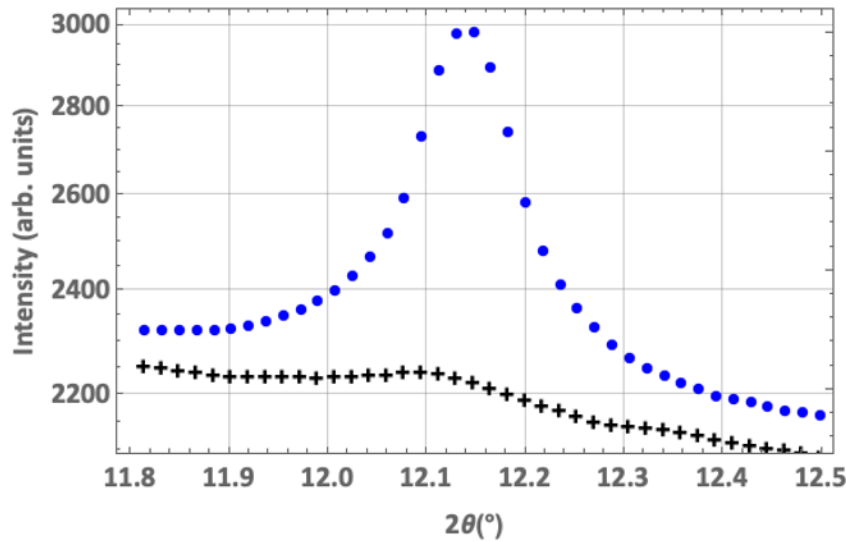


Figure 6: Comparison of Ge 111 diffraction peak intensity after full annealing cycle for sample W11 (POR thin film) and sample W9 (POR patterned array of lines).

Figure 7 shows a comparison of the temperature evolution of Ge111 and GST200 integrated intensities for samples W11 and W9. The reduced number of data points for W9 arises from the necessary increase in counting time (the ramp stays the same at 2°C/minute). As was already discussed, W11 shows a clear difference in behavior for the two phases: Ge crystallizes first at 340°C and GST crystallizes later at 370°C. Despite the low intensity and the reduced number of data points it is clear from figure 7 that W9 shows the same behavior with very similar crystallization temperatures: 340°C for Ge and 370°C for GST.

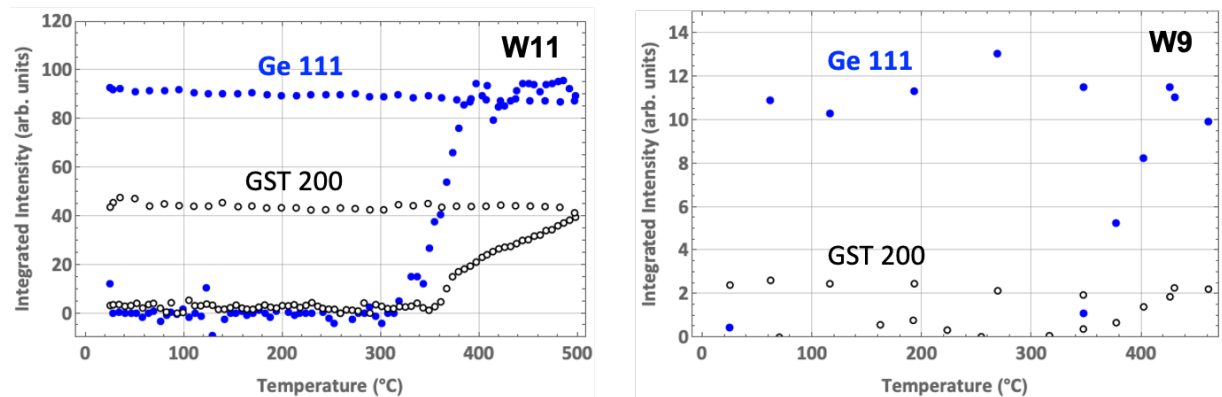


Figure 7: Integrated intensity of Ge 111 and GST 200 as a function of temperature for sample W11 (POR thin film) and sample W9 (POR patterned array of lines).

The evolution of interplanar distances $d^{\text{Ge}_{111}}$ as a function of temperature is linear for both samples and allows one to extract an effective perpendicular thermal expansion coefficient. The GST200 peak is too weak in sample W9 to allow for a reliable extraction of peak position. The effective perpendicular thermal expansion coefficients are respectively $9.9 \times 10^{-6} \text{ K}^{-1}$ and $4.8 \times 10^{-6} \text{ K}^{-1}$ for W11 and W9. Hence a clear difference in thermoelastic behavior is

evidenced. The value for W9 is close to what is expected for Ge lines confined within SiN lines, using the approximation developed in [19] for volume averaged stress in a damascene structure : $4.9 \times 10^{-6} \text{ K}^{-1}$.

3°) Influence of N content

The three patterned samples (W1 POR-2%N, W9 POR, W12 POR+2%N) have been thermally cycled between room temperature and 500°C. Nitrogen doping results in a significant reduction in the intensity of Ge 111 diffraction peak as evidenced in figure 8 (left hand side). In addition, the average domain size extracted from Ge 111 FWHM decreases from 26 nm (W1-POR-2%N) to 18 nm (W9-POR) and even down to 5 nm (W12-POR+2%N). At the same time no significant evolution of domain size is observed from GST 200.

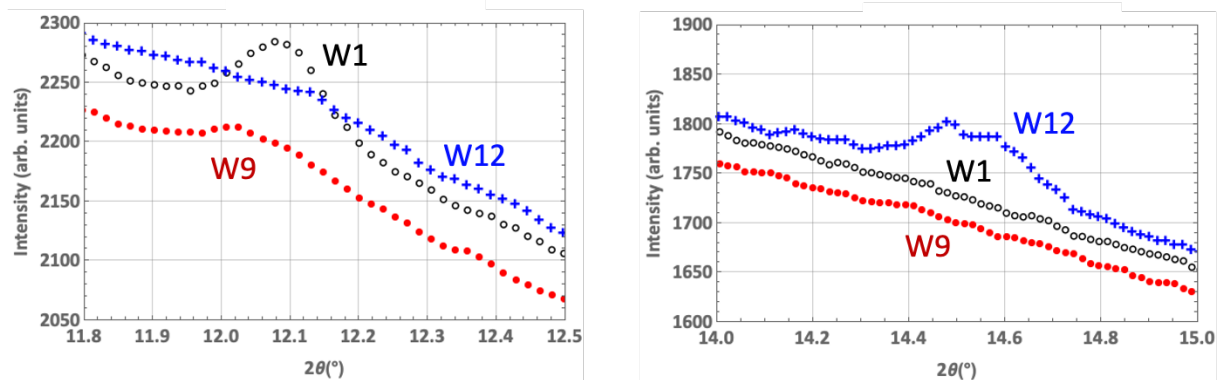


Figure 8: Comparison of selected areas of diffraction patterns at 450°C for samples W1 (POR-2%N), W9 (POR) and W12 (POR+2%N). The left hand side shows Ge 111 diffraction peak. Right hand side shows the region between $2\theta = 14^\circ$ and $2\theta = 15^\circ$ where Ge nitride most intense peaks might be expected.

Moreover, a broad diffraction peak appears around 14.5° for sample W12, which is the most highly doped sample. This angle corresponds to an interplanar spacing of 2.73 \AA , which correspond to strong diffraction lines of α and $\beta \text{ Ge}_3\text{N}_4$ [20]. A broad diffraction in the same zone of reciprocal space has been reported for germanium nitride films prepared by RF sputtering [21]. N is known to favorably bond with Ge [22,23] in PCMs through GeN_x formation. This has already been observed in stoichiometric amorphous $\text{Ge}_2\text{Sb}_2\text{Te}_5$ thin films [24]. Introduction of N in Ge-rich GST has been shown to slow down the phase separation and crystallization processes of both Ge and GST phases [25, 26], and to reduce the average grain size of crystallized phases [27], in agreement with our findings.

Conclusions

We have investigated the crystallization behavior of thin films and patterned structures of GST- θ material capped with SiN, using *in-situ* synchrotron x-ray diffraction at DiffAbs beamline (SOLEIL synchrotron). The as-deposited structures are amorphous. After crystallization a mixture of Ge and GST is observed with no noticeable texture. It is remarkable that Ge crystallizes before GST (15°C difference in crystallization temperature). Ge crystallization is followed by grain growth, which occurs during GST crystallization. The analysis of effective thermal expansion upon cooling indicates that the thermoelastic

behavior is different between thin films and patterned structures and that it is dominated by Ge. Nitrogen doping strongly reduces Ge crystallization. In the sample with the highest doping level (POR+2%) a diffraction broad band that may be assigned to Ge₃N₄ is found after annealing.

Acknowledgments

We would like to thank SOLEIL synchrotron for allocating beamtime on DiffAbs beamline. Ph. Joly (Synchrotron SOLEIL, DiffAbs) is thanked for technical support. IPCEI/Nano 2022 program is acknowledged for partial funding of this work.

References

- [1] HSP Wong, S. Raoux, S. Kim, JL Liang, JP Reifenberg, B. Rajendran, M. Asheghi, KE Goodson, Proc. Of the IEEE 98, 2201 (2010).
- [2] R. F. Freitas and W. W. Wilcke, IBM J. Res. Dev. 52, 439 (2008).
- [3] G. W. Burr, B. N. Kurdi, J. C. Scott, C. H. Lam, K. Gopalakrishnan, and R. S. Shenoy, IBM J. Res. Dev. 52, 449 (2008).
- [4] D. J. Wouters, R. Waser, and M. Wuttig, Proc. IEEE 103, 1274 (2015).
- [5] P. Zuliani, E. Palumbo, M. Borghi, G. Dalla Libera, R. Annunziata, Solid State Electronics 111, 27 (2015).
- [6] A. Fantini *et al.*, in 2010 International Electron Devices Meeting, 2010, 29.1.1-29.1.4.
- [7] R. Fallica, E. Varesi, L. Fumagalli, S. Spadoni, M. Longo, C. Wiemer, Physica Status Solidi (RRL) – Rapid Research Letters 7, 1107 (2013).
- [8] T. Nirschl *et al.*, in 2007 IEEE International Electron Devices Meeting, 2007, 461–64.
- [9] Y. Yin, H. Zhang, S. Hosaka, Y. Liu and Q. Yu, Journal of Physics D: Applied Physics 46, 505311 (2013).
- [10] P. Pangaud, S. Basolo, N. Boudet, J.F. Berar, B. Chantepie, J.C. Clemens, P. Delpierre, B. Dinkespiler, K. Medjoubi, S. Hustache, M. Menouni, and C. Morel, Nucl. Instruments Methods Phys. Res. Sect. A Accel. Spectrometers, Detect. Assoc. Equip. 591, 159 (2008).
- [11] C. Mocuta, M.I. Richard, J. Fouet, S. Stanescu, A. Barbier, C. Guichet, O. Thomas, S. Hustache, A. V. Zozulya, and D. Thiaudière, J. Appl. Crystallogr. 47, 482 (2014).
- [12] T. Matsunaga, N. Yamada, and Y. Kubota, Acta Crystallogr. Sect. B Struct. Sci. 60, 685 (2004).
- [13] R. R. Reeber and K. Wang, Materials Chemistry and Physics 2–3, 259 (1996).
- [14] IM. Park, JK. Jung, SO. Ryu, KJ. Choi, BG. Yu, IB. Park, SM. Han, YC. Joo, Thin Solid Films 517, 848 (2008).
- [15] G.K. Williamson and W.H. Hall, Acta Metallurgica 1, 22 (1953).
- [16] O. Thomas, S. Labat, T. Cornelius, MI. Richard, in Rayons X et matière - Volume 6 edited by Philippe Goudeau and René Guinebretière, ISTE Editions, to be published (2021).
- [17] R. Cecchini, K. Kohary, A. Fernández, M. Cabibbo, and A. Marmier, J. Phys. Chem. C 120, 5624 (2016).
- [18] O. Thomas, unpublished results.
- [19] LB. Freund and S. Suresh, Thin Film Materials: Stress, defect Formation and Surface Evolution, Cambridge University Press, 2003, p. 209.
- [20] S. Ruddlesden, P. Popper, Acta Cryst. 11, 465 (1958).
- [21] G. Maggioni, S. Carturan, L. Fiorese, N. Pinto, F. Caproli, D.R. Napoli, M. Giarola, G. Mariotto, Appl. Surf. Sci. 393, 119 (2017).

- [22] K.-H. Kim, J.-C. Park, J.-H. Lee, J.-G. Chung, S. Heo, S.-J. Choi, *Jpn. J. Appl. Phys.* 49, 101201 (2010).
- [23] Y. Kim, J. H. Baeck, M.-H. Cho, E. J. Jeong, D.-H. Ko, *J. Appl. Phys.* 2006, 100, 083502
M.C. Jung, Y.M. Lee, H.D. Kim, M.G. Kim, H.J. Shin, K.H. Kim, S.A. Song, H.S. Jeong, C.H. Ko,
and M. Han, *Appl. Phys. Lett.* 91, 89 (2007).
- [24] M.A. Luong, D. Wen, E. Rahier, N. Ratel Ramond, B. Pecassou, Y. Le Friec, D. Benoit, and
A. Claverie, *Phys. Status Solidi - Rapid Res. Lett.* 2000443, 1 (2020).
- [25] G. Navarro, V. Sousa, P. Noe, N. Castellani, M. Coue, J. Kluge, A. Kiouseloglou, C.
Sabbione, A. Persico, A. Roule, O. Cueto, S. Blonkowski, F. Fillot, N. Bernier, R. Annunziata,
M. Borghi, E. Palumbo, P. Zuliani, and L. Perniola, in *2016 IEEE 8th International Memory
Workshop (IMW)* (IEEE, Paris, France, 2016), pp. 1–4.
- [26] S. Privitera, E. Rimini, R. Zonca, *Appl. Phys. Lett.* 85, 3044 (2004).
- [27] L. Cheng, L. Wu, Z. Song, F. Rao, C. Peng, D. Yao, B. Liu, and L. Xu, *Journal of Applied
Physics* 113, 044514 (2013).